processes

MDPI

Article

Estimation of Thermophysical Properties as Functions of Temperature in Rapid Radial Solidification of Metallic Alloys

Remon Basily, Ahmed M. Teamah *, Mohamed S. Hamed and Sumanth Shankar

Department of Mechanical Engineering, McMaster University, Hamilton, ON L8S4L7, Canada; hamedm@mcmaster.ca (M.S.H.); shankar@mcmaster.ca (S.S.)
* Correspondence: teamaha@mcmaster.ca; Tel.: +1-905-920-6960

Abstract

Recent global efforts to produce lightweight electrified vehicles have motivated the push toward advanced lightweight materials which led to the creation of novel alloys optimized for use in high-pressure die casting (HPDC). HPDC enables the fabrication of near-net-shape automotive parts, significantly reducing or eliminating additional machining steps. A key feature of HPDC is the extremely fast cooling that forces the alloy to solidify within only a few seconds. Because of these rapid cooling conditions, it becomes essential to accurately evaluate the thermophysical behavior of newly designed lightweight alloys during severe quenching. Precisely quantifying these material properties is crucial for properly controlling HPDC operations and for building reliable numerical models that simulate filling and solidification. The thermophysical characteristics of such alloys vary markedly with temperature, especially when the material undergoes the fast solidification typical of HPDC. Therefore, understanding how these properties change with temperature during intense cooling becomes a critical requirement in alloy development. To address this need, a dedicated experimental system was designed to solidify molten metal samples under controlled and variable cooling conditions by applying multiple impinging water jets. An inverse heat-transfer algorithm was formulated to extract temperature-dependent thermal conductivity and diffusivity of the alloy as it solidifies under rapid cooling. To verify the reliability of both the inverse model and the measurements, experiments were performed using pure Tin, a reference material with well-documented thermophysical properties. The computed thermophysical properties of Tin were benchmarked against values reported in the literature and demonstrated reasonable consistency, with a maximum deviation of 13.6%.

Keywords: solidification of metallic alloys; thermophysical properties of metallic alloys; thermal diffusivity of metallic alloys; thermal conductivity of metallic alloys; high cooling rates of alloys; temperature-dependent properties of alloys

check for updates

Academic Editor: Yanzhong Li

Received: 8 November 2025
Revised: 29 November 2025
Accepted: 3 December 2025
Published: 5 December 2025

Citation: Basily, R.; Teamah, A.M.; Hamed, M.S.; Shankar, S. Estimation of Thermophysical Properties as Functions of Temperature in Rapid Radial Solidification of Metallic Alloys. *Processes* **2025**, *13*, 3939. https://doi.org/10.3390/pr13123939

Copyright: © 2025 by the authors. Licensee MDPI, Basel, Switzerland. This article is an open access article distributed under the terms and conditions of the Creative Commons Attribution (CC BY) license (https://creativecommons.org/licenses/by/4.0/).

1. Introduction

In recent years, the adoption of electric vehicles (EVs) has experienced a significant surge, driven by a confluence of environmental concerns, technological advancements, and government initiatives aimed at prioritizing sustainable transportation solutions. Modern cars come in various electric vehicle designs, including battery electric vehicles (BEVs), plug-in hybrid electric vehicles (PHEVs), and their variations. According to long-term projections, electric vehicle (EV) adoption is expected to increase gradually, reaching 68.4% of global vehicle sales by 2035 [1]. Governments worldwide have implemented stringent

emissions regulations and offered incentives to accelerate the transition to EVs, not only to reduce greenhouse gas emissions but also to mitigate reliance on fossil fuels and enhance energy security. Canada, as one of the world's leading economies, aims to achieve a net-zero emissions status by 2050. Rapid electrification of the country's transportation sector is imperative to meeting this ambitious goal [2]. By 2030, the United States aims to have 50% of all new light-duty cars be emission-free [3]. In the UK, traditional light-duty Internal Combustion Engine Vehicles (ICEVs) will be gradually replaced and phased out by 2030. Furthermore, starting in 2040, all newly sold Heavy Goods Vehicles (HGVs) must be zero-emission vehicles [4].

This shift has sparked innovation in materials science, particularly in the development of lightweight alloys and composites within the burgeoning electric car industry [5,6]. Manufacturers are investing in advanced alloys with exceptional strength-to-weight ratios, crucial for enhancing EV performance and range. Simultaneously, advancements in material science, manufacturing processes, and design techniques are accelerating the development of lightweight castable materials for the automotive industry. Ongoing research and collaboration involving scientists, engineers, and automotive manufacturers aim to create innovative materials that meet safety, durability, and cost considerations. These lightweight materials have the potential to revolutionize the automotive industry by making vehicles more fuel-efficient, eco-friendly, and performance-oriented while ensuring passenger safety.

Determining thermophysical properties is crucial for characterizing and effectively utilizing these new lightweight castable materials, providing valuable insights into their thermal behavior and performance for various applications. One of these applications is High Pressure Die Casting (HPDC), which offers significant benefits by facilitating the production of near-net-shape components. A fundamental aspect of HPDC is its capacity for rapid solidification. Hence, understanding the impact of the high cooling rates associated with HPDC on the thermophysical properties of new alloys is imperative. This understanding plays a pivotal role in developing precise filling and solidification models, thereby enabling the seamless incorporation of these alloys into commercial production via HPDC.

Several innovative approaches have been devised to determine the thermophysical properties of materials; however, it is important to note that these methods and devices may have certain limitations regarding the control of cooling rates, sample geometries, or temperature ranges. Differential Scanning Calorimetry (DSC) is commonly used to study the specific heat capacity of metal alloys. However, accurately determining the thermal properties solely based on composition using DSC can be challenging due to the lack of direct measurement of diffusivity and conductivity [7,8].

The Phoenix calorimeter is a specialized type of calorimeter. Its primary purpose is to investigate heat flow and thermal properties in substances. This instrument can effectively determine heat capacity; however, it is important to note that its sample size and temperature range have limitations [9].

The Laser Flash Technique (LFT) can effectively measure the thermal diffusivity and conductivity of materials, but it has several limitations. Firstly, LFT requires small, thin, and flat samples with uniform thickness, making this technique less suitable for complex geometries or larger-sized samples. Secondly, it assumes sample homogeneity and isotropy, which means consistent properties throughout; however, structural variations that inherently exist may affect this assumption. Thirdly, LFT is typically performed at high temperatures, limiting its suitability for low temperatures and materials with temperature-sensitive properties. Fourthly, it provides a single-point measurement at a specific temperature, lacking spatial resolution or temperature-dependent data required to understand the effect of cooling

rates. Additionally, the data analysis assumes pure conduction and neglects other heat transfer modes, potentially leading to inaccurate results. Lastly, LFT is best suited for solid materials with low to medium thermal conductivity, making it challenging or imprecise for highly conductive or low thermal diffusivity materials [10,11].

Numerous studies have investigated the Transient Plane Source (TPS) technique, and their findings have revealed that it requires thin and uniform samples, as deviations in thickness can impact measurement accuracy [12,13]. TPS is typically performed within a limited temperature range, making it unsuitable for extreme temperature conditions. It is more suitable for small-sized samples, as larger samples may introduce errors due to heat transfer effects at the edges. Good thermal contact between the sample and sensor is crucial, as any air gaps or imperfect contact can affect measurement accuracy. TPS provides a single-point measurement at a specific temperature and does not provide spatial or temperature-dependent data, requiring multiple measurements for a thermal property profile. Additionally, the technique assumes isotropic and homogeneous materials, limiting its accuracy for anisotropic materials with varying thermal properties in different directions.

At the nanoscale level, the Scanning Thermal Microscopy (SThM) method offers high-resolution thermal imaging, albeit limited by the probe tip size, making it less suitable for studying extremely small features or nanoscale structures [14,15]. SThM requires direct contact with flat and smooth sample surfaces, as rough or uneven surfaces can hinder accuracy. Probe tip material and geometry impact results, introducing complexities like heat dissipation and thermal resistance. Calibration and sophisticated data interpretation are necessary to establish accurate thermal properties, with potential uncertainties and errors. SThM measurements are time-consuming due to the scanning process, hindering the acquisition of large-scale thermal property maps quickly, especially with high spatial resolution. The guarded and the longitudinal heat flow techniques are conducted under steady-state conditions to measure thermal conductivity, best suited for materials with a low to medium range of thermal conductivity [16,17].

In [18], they introduced an analytical method that employs the Laplace Transform to estimate both thermal diffusivity and thermal conductivity. The thermal conductivity is determined from the heat flux obtained using a thin stainless steel heater, while specific formulas were derived for particular boundary conditions. The periodic temperature method is particularly suitable for estimating the thermophysical properties of composite materials with thicknesses ranging from 1 to 10 mm. In the case of paraffin/graphite material, this method was effectively employed using sinusoidal signals [19,20] to obtain accurate estimations.

The study in [21–23] proposed a numerical model to estimate the thermophysical properties of metals, independently of temperature. Materials data-driven modeling is a powerful approach used to estimate thermophysical properties, offering numerous advantages. It provides valuable insight into the relationships between material properties and their underlying structure and composition [24–26]. However, it is important to consider some limitations. Understanding the confidence level of the data-driven model is crucial; some data-driven models may lack transparency and physical interpretability, making it challenging to gain insights into the underlying physical mechanisms [27].

This study aims to establish an experimental methodology based on inverse heat transfer principles for estimating thermophysical properties across varying temperatures and under high cooling rates during the solidification of metallic alloy samples. Furthermore, it validates the accuracy of the experimental setup and procedure using pure Tin samples, which is a well-characterized material.

2. Methodology

2.1. The Proposed Inverse Heat Transfer Algorithm

The developed inverse heat transfer algorithm estimates the thermal diffusivity and thermal conductivity of an alloy sample placed inside a cylindrical steel mold through a single experiment. The inverse algorithm estimates the thermal diffusivity and thermal conductivity by minimizing the sum of squares error between the measured temperatures and the numerically calculated temperatures. The sample radius-to-height ratio R_{Alloy}: H is 1:13. According to [28], this ratio ensures radial heat transfer. The measured temperatures are obtained by using thermocouples positioned within the alloy sample (T1, T2, and T3) and the mold (T4, T5, and T6), as shown in Figure 1.

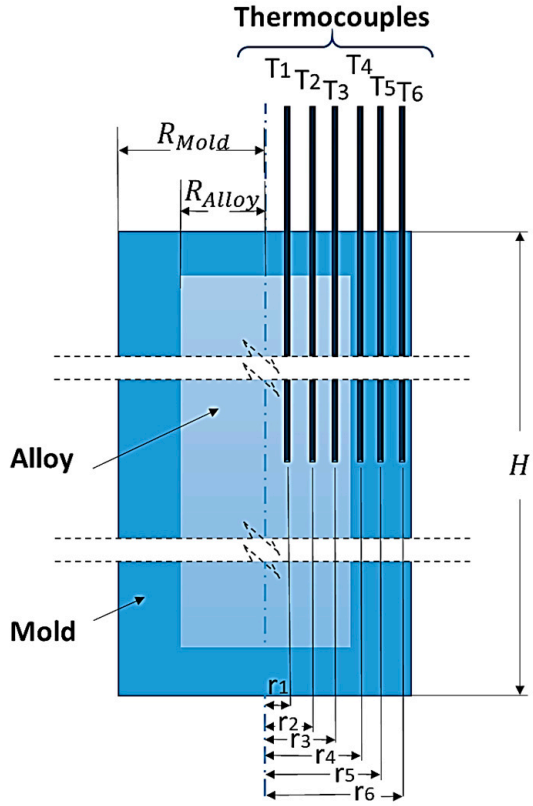


Figure 1. Schematic of the mold and alloy sample showing the positions of used thermocouples [29].

The inverse algorithm consists of a four-stage iterative process, depicted in Figure 2. The estimation begins with setting up the initial temperature condition. Subsequently, the algorithm estimates the thermal diffusivity (α) of the alloy sample and the interface temperature between the mold and the sample. The algorithm then estimates the heat flux at the interface using a temperature gradient estimated from the temperature measurements taken within the mold. Finally, the algorithm utilizes the estimated surface heat flux along with the thermal diffusivity and the interface surface temperature to estimate the thermal conductivity (k) of the alloy sample, utilizing temperature measurements taken within the alloy sample. Subsequently, the estimated value of α and k at the average temperature for each time step is considered. This process involves updating the initial temperature for the subsequent time step, allowing the estimation of α and k as functions of temperature.

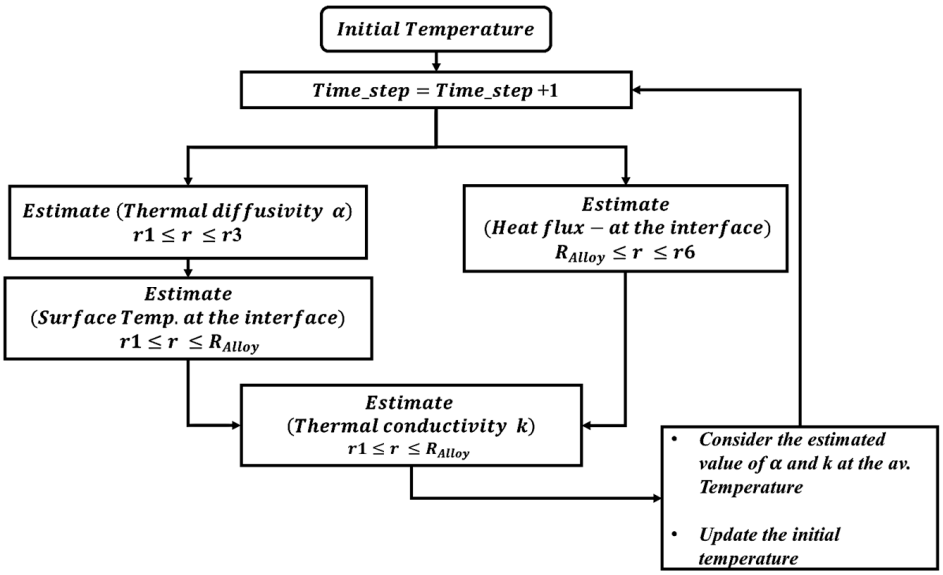


Figure 2. Flowchart of the main steps involved in the developed inverse algorithm [29].

2.2. Estimating the Thermal Diffusivity

The thermal diffusivity of the alloy sample is estimated using a numerical search technique that relies on the golden ratio and is defined as the Successive Reduction Method (SRM). The SRM involves adjusting the assumed thermal diffusivity value to minimize the sum of squares differences between the experimentally measured temperatures T1, T2, and T3 and temperatures calculated using a numerical model. The numerical model is based on the finite difference method (FDM) and solves unsteady heat transfer in the radial direction within the domain [r1:r3], governed by the conduction heat Equation (1). The initial temperature distribution is approximated using a polynomial function, with its degree determined by the number of measured temperature points minus one, as illustrated in Equation (2). In the example shown in Figure 1, N = 3 − 1 = 2. The boundary conditions used are prescribed temperatures, as illustrated in Equations (3) and (4).

$$\frac{1}{r}\frac{\partial}{\partial r}\left(r\frac{\partial T}{\partial r}\right) = \frac{1}{\alpha_{Alloy}}\frac{\partial T}{\partial t}, \qquad r1 \le r \le r3 \tag{1}$$

$$T(r,0) = \Sigma_{j=0}^{N} a_j r^j \tag{2}$$

$$T(r1,t) = \mathrm{T1} \tag{3}$$

$$T(r3,t) = \mathrm{T3} \tag{4}$$

The flowchart of the property estimation algorithm is shown in Figure 3. θ is any general unknown value that is assumed in the range [a, b], e.g., for the thermal diffusivity α_{Alloy}. The width of this range primarily influences computational costs rather than estimation accuracy. For the estimating process, intervals within this range are progressively narrowed down. Within the [a, b] range, internal values γ and δ are chosen relative to the golden ratio, ω.

$$\omega = \frac{\sqrt{5}+1}{2} \tag{5}$$

The sum of squares differences, G, between experimentally and numerically determined temperatures by (FDM) for $\theta = \gamma$ and $\theta = \delta$ is computed at each iteration, as expressed in Equation (6).

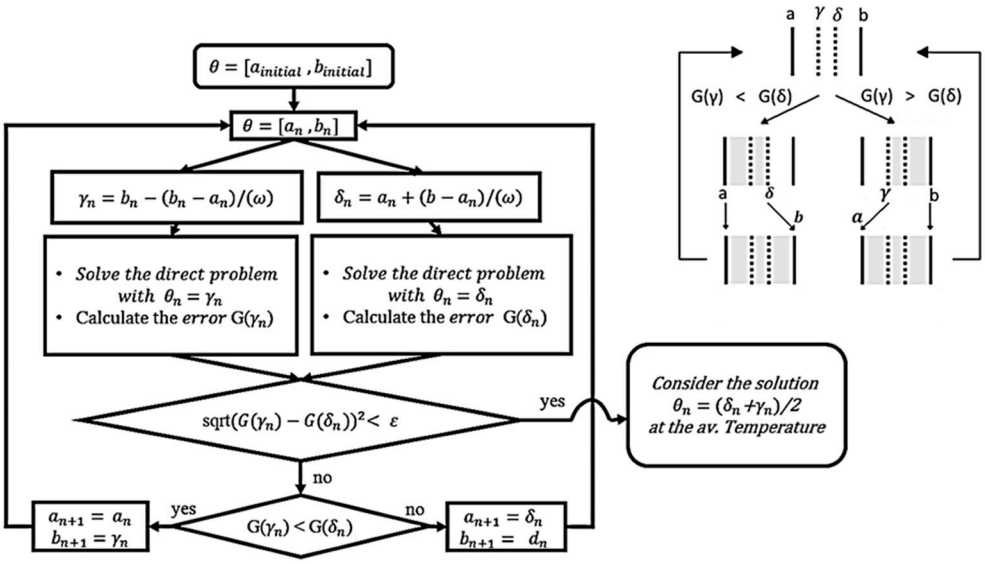


Figure 3. Detailed flowchart displaying the algorithm employed for the property estimation [29].

$$G = \sum([\mathrm{T2}] - [T^{FDM}|_{r=r2}])^2 \tag{6}$$

Intervals are updated based on error values G(γ) and G(δ). At each iteration, if G(γ) < G(δ), the interval [δ:b] is eliminated, and the interval is reduced to [a:δ]. If G(γ) > G(δ), the interval [a:γ] is eliminated, and the interval is reduced to [γ:b]. This refining process continues until a single value within a small threshold ($\varepsilon = 10^{-9}$) is converged. This threshold serves as the stopping criterion at each time step. Then the value of $\theta_n = (\delta_n + \gamma_n)/2$ is considered the estimated value for the current time step.

2.3. Estimating Interface Temperature Between the Mold and Sample

The same SRM is used to estimate the interface temperature T_S on the alloy domain. In this case, the unknown parameter θ is the interface temperature. Equation (7) governs the numerical model. The initial temperature distribution is approximated using a polynomial function, with its degree determined by the number of measured temperature points [T1, T2, and T3] minus one, as illustrated in Equation (8). In the example shown in Figure 1, N = 3 − 1 = 2. The boundary conditions used are prescribed temperatures, as illustrated in Equations (9) and (10), since the boundary condition at R_{Alloy} is T_S the value to be estimated in this stage.

$$\frac{1}{r}\frac{\partial}{\partial r}\left(r\frac{\partial T}{\partial r}\right) = \frac{1}{\alpha_{Alloy}}\frac{\partial T}{\partial t}, \qquad r1 \le r \le R_{Alloy} \tag{7}$$

$$T(r,0) = \sum_{j=0}^{N} a_j r^j \tag{8}$$

$$T(r1,t) = \mathrm{T1} \tag{9}$$

$$T(R_{Alloy},t) = T_S = \theta \tag{10}$$

The sum of squares differences, G, between experimentally and numerically determined temperatures is expressed in Equation (11).

$$G = \sum([\mathrm{T2,T3}] - [T^{FDM}|_{r=r2},\ T^{FDM}|_{r=r3}])^2 \tag{11}$$

2.4. Estimating the Heat Flux at the Interface

The interface heat flux, q_{est}, is estimated utilizing the same algorithm as depicted in Figure 3, with the unknown value θ being the heat flux at the interface. The numerical model is governed by Equation (12). The initial temperature distribution is approximated using a polynomial function, with its degree determined by the number of measured temperature points [T4, T5, and T6] minus one, as illustrated in Equation (13). In the example shown in Figure 1, N = 3 − 1 = 2. The heat flux at the interface requiring estimation is applied as a boundary condition using Equation (14). The second boundary condition is a prescribed temperature, as illustrated in Equation (15).

$$\frac{1}{r}\frac{\partial}{\partial r}\left(r\frac{\partial T}{\partial r}\right) = \frac{1}{\alpha_{Mold}}\frac{\partial T}{\partial t}, \qquad R_{Alloy} \le r \le r6 \tag{12}$$

$$T(r,0) = \Sigma_{j=0}^{N} a_j r^j \tag{13}$$

$$-k_{Mold}\frac{\partial T}{\partial r}|_{r=R_{Alloy}} = q_{est} = \theta \tag{14}$$

$$T(r6,t) = \mathrm{T6} \tag{15}$$

The sum of squares differences, G, between experimentally and numerically determined temperatures is expressed in Equation (16).

$$G = \sum([\mathrm{T4},\mathrm{T5}] - [T^{FDM}|_{r=r4},\ T^{FDM}|_{r=r5}])^2 \tag{16}$$

2.5. Estimating the Thermal Conductivity

The estimation of the thermal conductivity is carried out using the SRM depicted in Figure 3, with the unknown value θ being the thermal conductivity of the alloy, k_{Alloy}. The numerical model is governed by Equation (17). The initial temperature distribution is approximated using a polynomial function, with its degree determined by the number of measured temperature points [T1, T2, and T3] minus one, as illustrated in Equation (18). In the example shown in Figure 1, N = 3 − 1 = 2. The estimated heat flux at the interface is applied as a boundary condition using Equation (19). The second boundary condition is a prescribed temperature, as illustrated in Equation (20).

$$\frac{1}{r}\frac{\partial}{\partial r}\left(r\frac{\partial T}{\partial r}\right) = \frac{1}{\alpha_{Alloy}}\frac{\partial T}{\partial t}, \qquad r1 \le r \le R_{Alloy} \tag{17}$$

$$T(r,0) = \sum_{j=0}^{N} a_j r^j \tag{18}$$

$$-k_{Alloy}\frac{\partial T}{\partial r}|_{r=R_{Alloy}} = q_{est} \tag{19}$$

$$T(r1,t) = \mathrm{T1} \tag{20}$$

The sum of squares differences, G, between experimentally and numerically determined temperatures is expressed in Equation (21).

$$G = \sum\left([\mathrm{T2},\mathrm{T3},\ Ts] - \left[T^{FDM}|_{r=r2},\ T^{FDM}|_{r=r3},\ T^{FDM}|_{r=R_{Alloy}}\right]\right)^2 \tag{21}$$

Table 1 summarizes the essential parameters used in the estimation algorithm. It includes estimated values (θ) along with their corresponding domains, boundary conditions, and the sum of squares differences (G) for each stage.

Table 1. Summary of Estimation Algorithm Parameters.

Estimated Value θ	Domain	Boundary Conditions	The Sum of Squares Differences, G
α_{Alloy}	$r1 \le r \le r3$	$T(r1,t) = \mathrm{T1}$ $T(r3,t) = \mathrm{T3}$	$\sum([\mathrm{T2}] - [T^{FDM}\mid_{r=r2}])^2$
T_S	$r1 \le r \le R_{Alloy}$	$T(r1,t) = \mathrm{T1}$ $T(R_{Alloy},t) = T_S$	$\sum([\mathrm{T2,T3}] - [T^{FDM}\mid_{r=r2},\ T^{FDM}\mid_{r=r3}])^2$
q_{est}	$R_{Alloy} \le r \le r6$	$-k_M \frac{\partial T}{\partial r}\mid_{r=R_A} = q_{est}$ $T(r6,t) = \mathrm{T6}$	$\sum([\mathrm{T4,T5}] - [T^{FDM}\mid_{r=r4},\ T^{FDM}\mid_{r=r5}])^2$
k_{Alloy}	$r1 \le r \le R_{Alloy}$	$T(r1,t) = \mathrm{T1}$ $-k_A \frac{\partial T}{\partial r}\mid_{r=R_A} = q_{est}$	$\sum([\mathrm{T2,T3,}\ Ts] - [T^{FDM}\mid_{r=r2},\ T^{FDM}\mid_{r=r3},\ T^{FDM}\mid_{r=R_A}])^2$

2.6. Validation of the Inverse Algorithm Using a Numerical (Virtual) Experiment

Two numerical simulations were conducted to validate the developed inverse algorithm. The simulations involved performing a direct numerical simulation using well-defined thermophysical properties sourced from the literature. A heat flux of 15,000 W/m^2 was being extracted from the outer surface of the mold, while time-dependent temperature measurements were taken at specific positions based on the numerical results of these simulations (T-1 to T-6), shown in Figure 4. Subsequently, the obtained temperature measurements were input into the inverse algorithm to estimate (k, and α). The algorithm was validated by comparing the estimated thermophysical properties obtained from the inverse solver with the input properties taken from the literature.

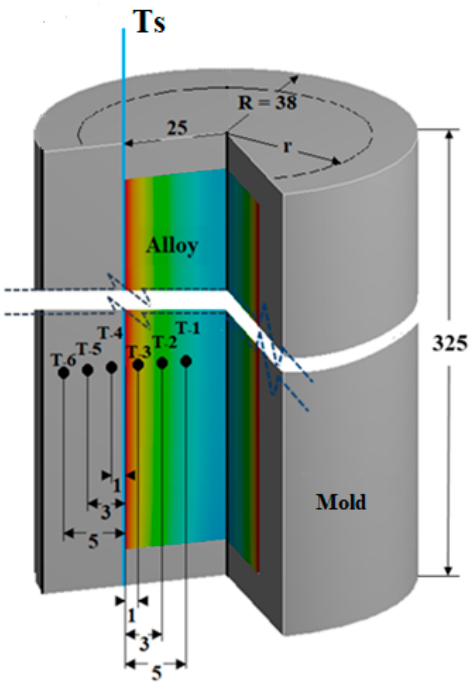


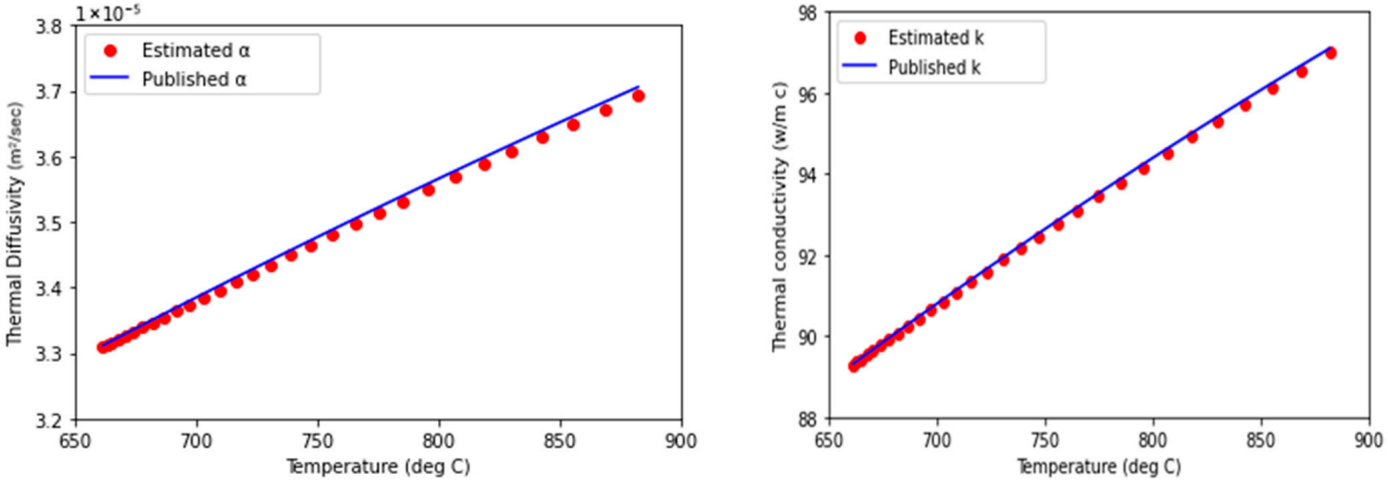
Figure 4. Geometry and thermocouple locations considered in numerical simulations (all dimensions are in mm) [29].

2.6.1. Estimating k and α of the Solid and Liquid Phases of High-Purity Aluminum

The temperature-dependent thermal conductivity and diffusivity of high-purity aluminum (99.999%) obtained from [30] were determined using an ohmic pulse-heating technique. Subsequently, a direct numerical simulation was conducted to generate the temperature distribution using those reference values. The resulting temperature distributions at the specified positions were then utilized by the inverse solver to estimate the thermal conductivity and diffusivity in both the liquid and solid phases.

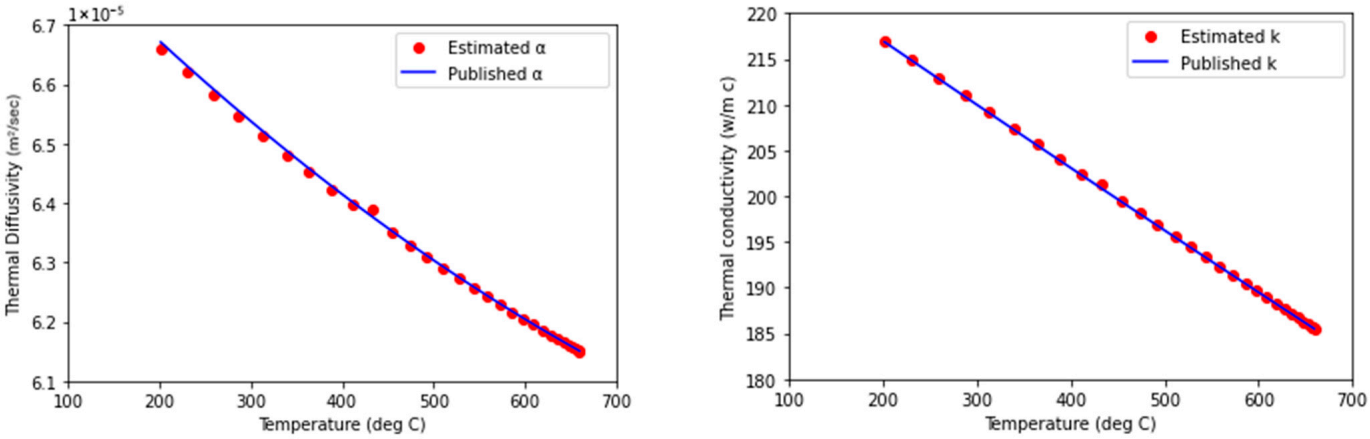
Figures 5 and 6 show a comparison between the estimated and the published values of α and k used as input in the numerical simulations. The results show a very good agreement. The root mean square error (RMSE) is used to provide a measure of the average deviation between the estimated and published values. Its formula is shown in Equation (22), where y represents the estimated values, $\hat{y}$ represents the published values, and m is the number of data points. Table 2 provides the root mean square error (RMSE) and the maximum difference between the estimated and the reference values for the temperature-dependent thermal conductivity and diffusivity.

$$RMSE = \sqrt{\frac{1}{m}\Sigma_{j=1}^{m}\left(y_j - \hat{y}_j\right)^2} \quad (22)$$



(**a**) Thermal diffusivity. (**b**) Thermal conductivity.

Figure 5. Comparison between the estimated and the input temperature-dependent liquid phase thermophysical properties [30] of pure Aluminum [29].



(**a**) Thermal diffusivity. (**b**) Thermal conductivity.

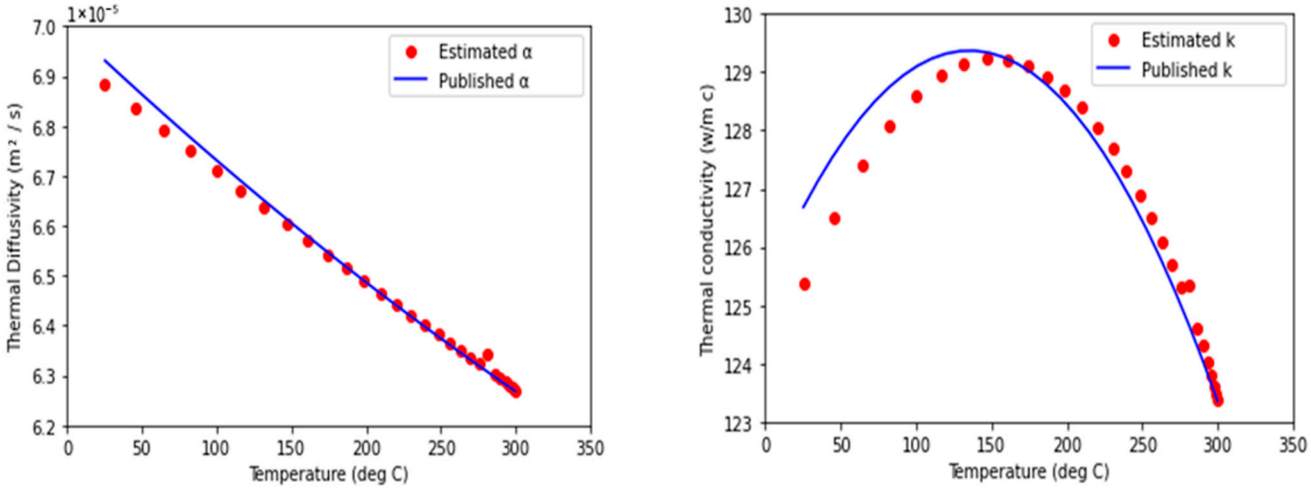
Figure 6. Comparison between estimated and input temperature-dependent solid phase thermophysical properties [30] of pure Aluminum [29].

Table 2. The maximum difference in the estimated α and k of high-purity aluminum in the liquid and solid phases.

	Thermal Diffusivity		Thermal Conductivity	
	(m^2/s)	**Maximum Difference %**	**(W·m/°C)**	**Maximum Difference %**
Liquid phase	8.41×10^{-8}	0.7	0.07	0.2
Solid phase	5.44×10^{-8}	0.3	0.09	0.023

2.6.2. Estimating the Thermophysical Properties of a Casting Magnesium Alloy

In [9], a magnesium casting alloy, Mg-Zn-Si-Ca, was specifically engineered to have superior thermal conductivity in the solid phase. The thermal diffusivity of the solid phase of this alloy was determined using the laser flash method, while the heat capacity was measured utilizing a Phoenix calorimeter [9]. Similar to the first case of pure Aluminum, the published temperature-dependent α and k were utilized as inputs to the direct numerical simulation, and the output temperatures were used as input to the developed inverse solver in order to evaluate its accuracy in estimating the magnesium alloy's properties. Figure 7 provides a comparison of the estimated thermal diffusivity and conductivity of the solid phase of the magnesium alloy as a function of temperature. The results demonstrate a good agreement. Table 3 presents the associated metrics for assessing the accuracy of the estimation, specifically the root mean square error (RMSE) and the maximum difference.



(**a**) Thermal diffusivity. (**b**) Thermal conductivity.

Figure 7. Comparison between the estimated and the input temperature-dependent liquid phase thermophysical properties [9] of the casting magnesium alloy [29].

Table 3. The maximum difference in the estimated α and k of the Mg-Zn-Si-Ca casting alloy.

	Thermal Diffusivity		Thermal Conductivity	
	(m^2/s)	**Maximum Difference %**	**(W·m/°C)**	**Maximum Difference %**
Mg-Zn-Si-Ca casting alloy	1.98×10^{-7}	0.72	0.54	1.02

3. Experimental Setup

The experimental setup developed and used in this study was devised to facilitate the monitoring of temperature variations during the rapid solidification of a cylindrical alloy sample placed inside a steel mold subjected to high cooling rates. The mold cooling

is achieved using an array of impinging water jets. The cooling rate can be varied by changing the water jet velocity. Utilizing a set of type-K thermocouples connected to a data acquisition system, temperature measurements were systematically acquired at specific locations within the alloy sample and within the mold. These temperature measurements constituted the input to the inverse solver in order to determine the temperature-dependent thermal diffusivity and thermal conductivity of the alloy sample under investigation. Figure 8 illustrates an overview of the experimental setup and methodology.

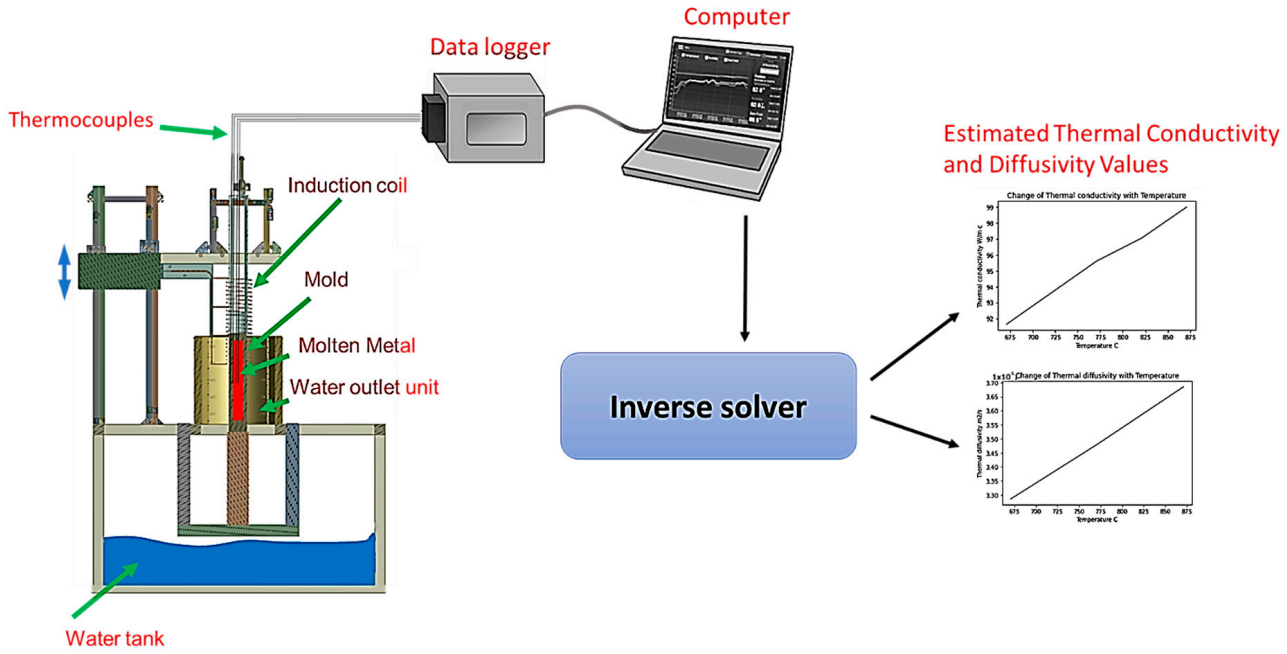


Figure 8. Experimental setup and methodology [29].

The experimental setup consists of an alloy sample, a cylindrical mold, an induction heating system, a water-jet cooling system, a shield tube with a moving mechanism, and temperature sensors connected to a data acquisition system. Figure 9 shows a schematic of the experimental setup. A photograph of the experimental setup is shown in Figure 10.

The cylindrical mold is made of the 4140 alloy steel. Its inner radius, outer radius, and height are 24, 33, and 320 mm, respectively. The mold was fabricated in two halves securely held together by fitted rings, as depicted in Figure 11. The mold dimensions were selected to establish a sample radius-to-height ratio of 1:13 to ensure one-dimensional heat transfer in the radial direction [28]. Sensor placement is arranged: the holes in the cap align with the layout outlined in Figure 12. Nine Thermocouples were placed within the mold, and the alloy sample was inside a set of protective tubes. The positions of these nine thermocouples are shown in Figure 12. The stainless-steel protection tubes were used to maintain thermocouple straightness and ensure they remained in their designated positions within the mold and the alloy sample.

The positioning of the thermocouples is determined by the positions of the protective tubes. The accuracy of the estimated α and k using the developed inverse solver depends on the accuracy of the thermocouples' positions. The actual positions were measured after completing a solidification experiment. A horizontal slice was cut through the solidified cylindrical sample at the same level where the thermocouples' tips were placed, as depicted in Figure 13. The black dots in Figure 13 represent the actual positions of the thermocouples placed within the sample. Image processing was carried out using ImageJ software (1.53v-Nov 2022) to analyze the photograph of the sample and precisely determine the

actual positions of the thermocouples placed within the sample. Table 4 lists the actual and designed thermocouples' positions.

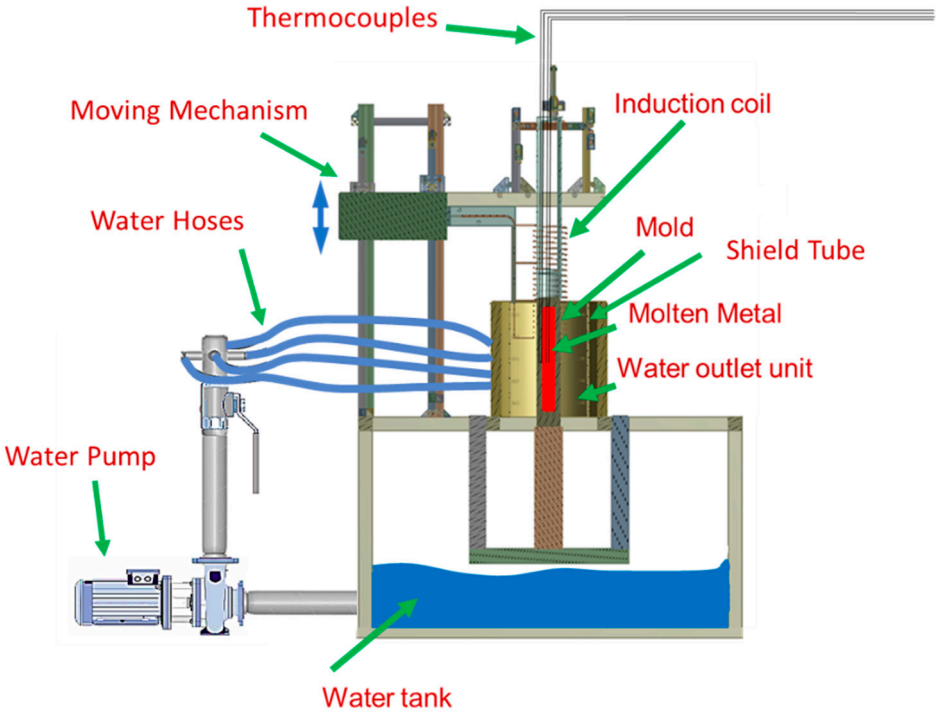


Figure 9. Schematic of the experimental setup [29].

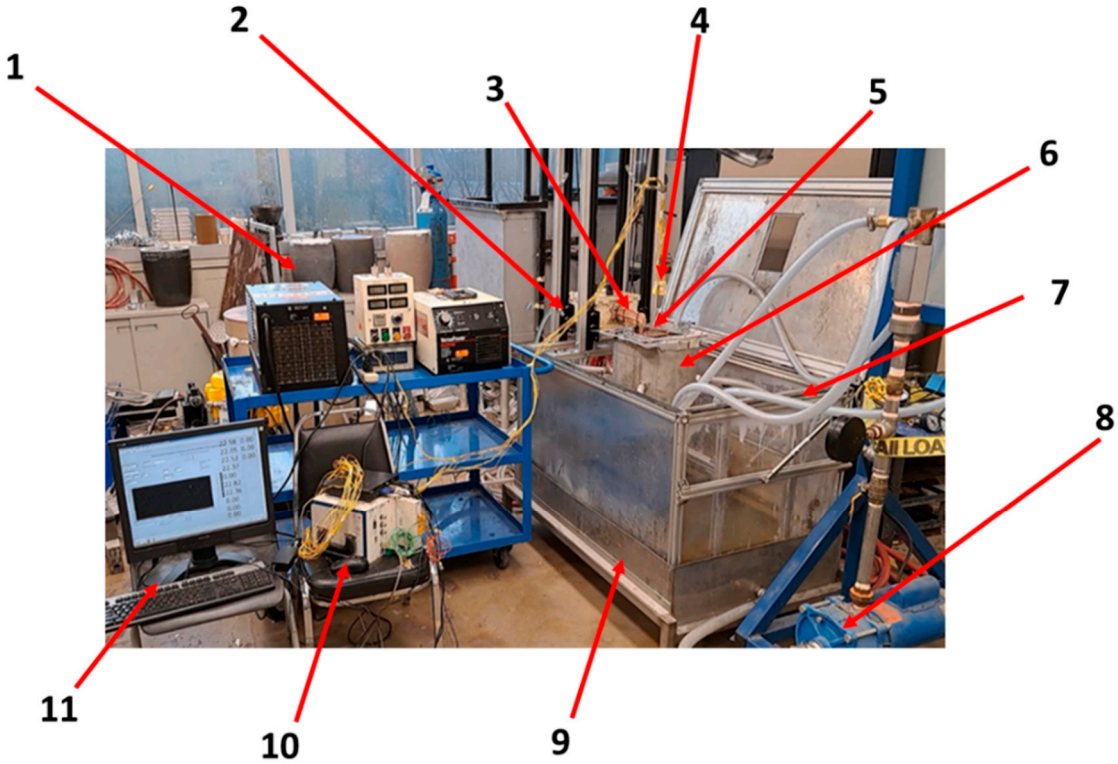


Figure 10. A Photograph of the experimental setup: (1) Induction Heating System, (2) Moving Mechanism, (3) Induction Coil, (4) Thermocouples, (5) Mold, (6) Water Outlet unit, (7) Water Hoses, (8) Water Pump, (9) Water Tank, (10) Data Acquisition, (11) Computer [29].

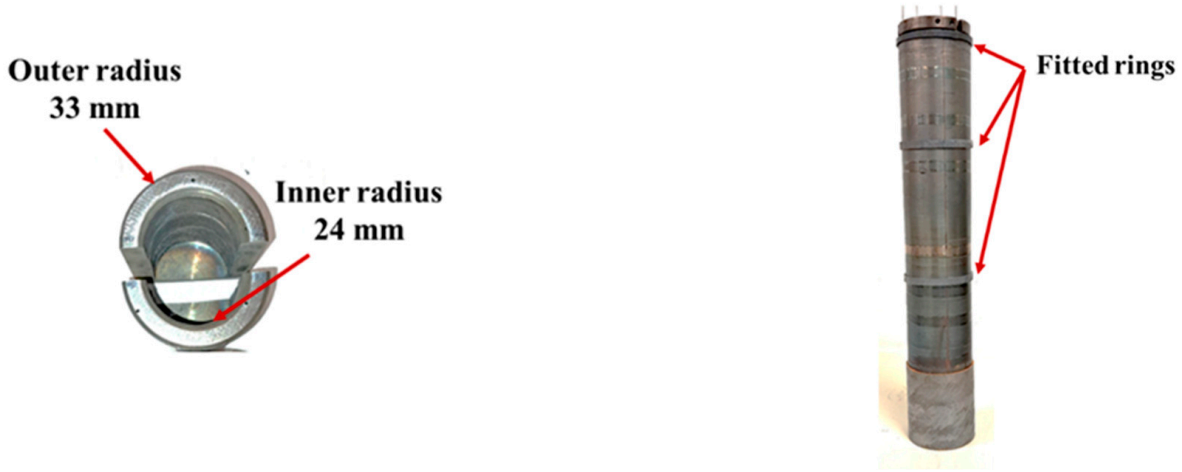


Figure 11. Details of the mold. (**a**) Two halves of the mold, and (**b**) Mold with fitted rings [29].

Thermocouple Number	Position in the radial direction from the center (mm)
1	0
2	10
3	18
4	20
5	22
6	26
7	28
8	30
9	26

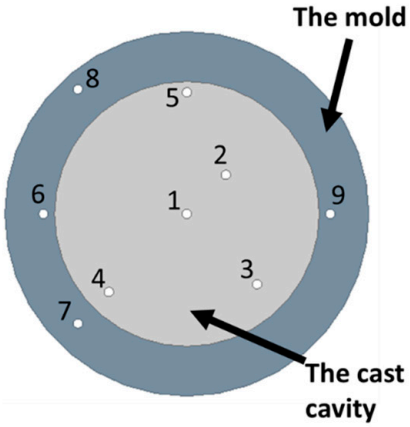


Figure 12. Positions of the thermocouples placed within the mold and alloy sample [29].

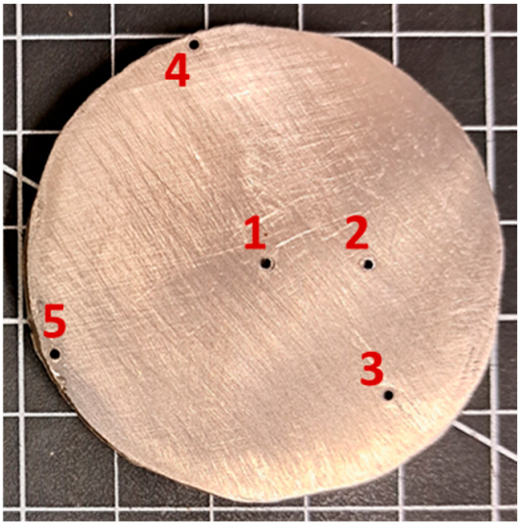


Figure 13. Slice of a solidified sample showing the actual positions of the thermocouples [29].

Table 4. Comparison of designed and actual thermocouple positions.

Thermocouple No.	Designed Position (mm)	Actual Position (mm)
1	0	0
2	10	10.25
3	18	17.93
4	20	22.9
5	22	23.3

The induction heating system manufactured by RADYNE consists of a 5 kW power supply along with a helical copper induction coil and a water chiller unit employed to cool the induction coil. The induction heating system provided a means of in situ heating of the alloy sample to the desired superheat temperature instead of pouring molten metal into the mold, which would create turbulence within the sample, which could affect the accuracy of the estimated thermophysical properties of the liquid phase. The water jet cooling system comprises several essential components selected to ensure efficient heat dissipation from the mold and sample. Water is applied with a centrifugal pump with a flow capacity of up to 2.6 L per second.

Water is fed into the water jacket through four inlets arranged around the jacket to ensure uniform distribution. The water jacket has five rings of water jets arranged vertically. Each ring has eight 6 mm diameter nozzles arranged around the mold circumference. Water flow is controlled by a gate valve and measured with a digital flow meter. The YFIXTOOL model EDFM-01, a 2-inch Digital Turbine Flow Meter, was employed for real-time monitoring of water flow, providing a flow rate range of 60–500 LPM.

The water jacket was made of two stainless steel cylinders with an inner and outer diameter of 254 mm and 305 mm, respectively. The two cylinders were joined together with top and bottom disks to form an annular space measuring 300 mm in height. Details of the water jacket are shown in Figure 14. The experimental methodology entails maintaining a continuous water jet stream both before the initiation of the cooling process and during the heating phase to ensure the attainment of steady-state and uniform water streams. To prevent water from reaching the mold during the heating phase, a stainless-steel shield tube, guided by two sliders, was employed. Upon the commencement of the cooling process, a locking device is utilized to release the shield tube rapidly by gravity. This action permits the water stream to impact the outer surface of the mold, initiating the quenching process.

The induction coil is placed around the mold during the heating phase and moved up before the start of the cooling phase. The movement of the induction coil is facilitated by a specifically constructed mechanism consisting of a moving rack connected to a counterweight, wire linkage, and two pulleys. This setup ensures a smooth and controlled movement of the induction coil. Temperature measurements are conducted using nine type K, 0.81 mm diameter ungrounded thermocouples with a time constant of 0.257 s, which are placed inside protection tubes to ensure precise placement. The protection tube is made from stainless steel with an inner and outer diameter of 1.32 mm and 1.57 mm, respectively. Temperature data is acquired at a rate of 100 readings per second using a National Instruments model SCXI-1000 data acquisition system.



Figure 14. Details of the water jacket, (**a**) Shows the water jacket horizontally, while (**b**) Reveals the cylindrical mold centered inside it [29].

4. Results and Discussion

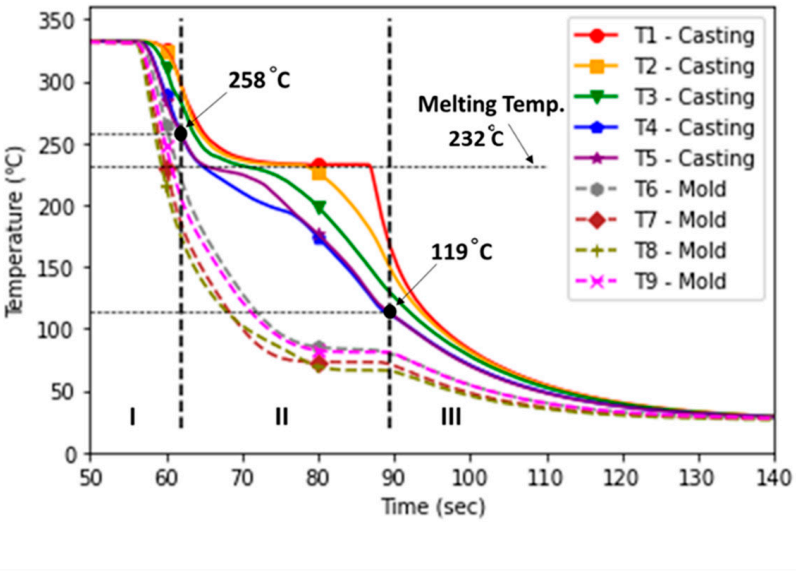
The experimental methodology employed in this study aimed to estimate the temperature-dependent thermal diffusivity and thermal conductivity for any alloy sample. To validate the accuracy of the experimental setup and the developed inverse algorithm, an experiment using pure Tin was carried out. Since the thermal diffusivity and conductivity are readily available in the literature, pure Tin was used as a benchmark material to assess the accuracy of the estimated thermophysical properties for both the solid and liquid phases.

Figure 15 shows cooling curves acquired during a typical solidification experiment. In this experiment: the initial sample temperature was 332 °C, the water temperature was 20 °C, and the average water jet velocity was 2.3 m/s. The maximum cooling rate reached 21 °C/s at the T5 position. The melting temperature of Tin is 231.92 °C. Thermocouples T6 and T9 are placed at the same radial position in the mold to ensure the uniformity of the cooling process. As shown in Figure 15, the cooling curves of T6 and T9 are in good agreement. The acquired data were divided into three distinct regions: (I) the liquid region, (II) the mushy zone, and (III) the fully solidified region. The time constant of the thermocouples is 0.257 s. Temperature readings were taken at a rate of one reading every 0.3 s from both the fully liquid and fully solid regions of the tin sample to estimate its thermal diffusivity and thermal conductivity.

To accurately understand the progression of solidification and the influence of latent heat at different thermocouple positions, the cooling curve obtained by thermocouple T5 was analyzed. T5 is the nearest thermocouple to the interface between the mold and the alloy sample. The T5 cooling curve is shown in Figure 16. The rate of change in temperature was calculated and included in Figure 16. The following key points have been identified from the T5 cooling curve during the solidification experiment:

- Point A indicates the beginning of rapid cooling, as the rate of the temperature change curve starts increasing rapidly in magnitude.
- At Point B, solidification begins as indicated by the start of the increase in the rate of temperature change until it reaches its maximum, caused by the release of latent heat during solidification.

- At Point C, solidification is complete at the T5 position, as indicated by the minimum value of the rate of temperature change before it begins to increase again, influenced by the release of latent heat from neighboring positions.
- At Point D, solidification effects and the influence of latent heat from adjacent positions come to an end, signified by the steady rate of temperature change.



Thermocouple Number	Position in the radial direction from the center (mm)
T1	0
T2	10.25
T3	17.93
T4	22.9
T5	23.3
T6	26
T7	28
T8	30
T9	26

Figure 15. Cooling curves obtained during a typical solidification experiment of pure Tin [29].

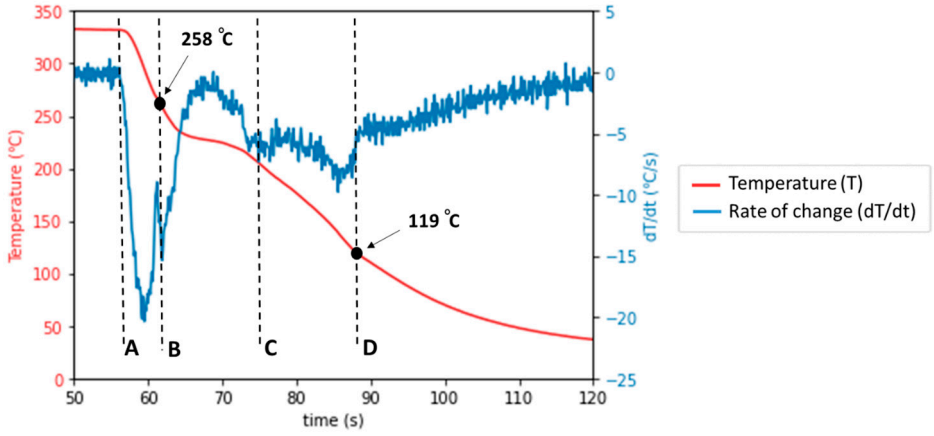


Figure 16. The cooling curve and cooling rate analysis of data obtained at position T5 [29].

Point B indicates the end of the fully liquid region at 258 °C, as solidification begins thereafter, progressing from the T5 position toward the center of the Tin sample. Similarly, point D indicates the commencement of the solid region, denoting the end of the solidification process and the latent heat transfer from the center of the sample towards the T5 position at 119 °C. These temperature points were used to divide the three distinct regions (I), (II), and (III) as shown in Figures 15 and 16.

The temperature data obtained from the nine thermocouples were input into the inverse solver to estimate the temperature-dependent thermal conductivity and diffusivity of both the liquid and solid phases of the Tin sample.

4.1. Estimation of Thermal Conductivity and Thermal Diffusivity for the Solid Phase

The temperature-dependent thermal conductivity in the solid phase was estimated and compared with the published data in [31–33]. The thermal conductivity values in [31]

were obtained through the Guarded Heat Flow, while those in [32,33] were obtained via the Longitudinal Heat Flow method. This comparison is depicted in Figure 17 and summarized in Table 5. The maximum deviation between the estimated thermal conductivity k and the published data falls within the range of +7.8% to −13.6%.

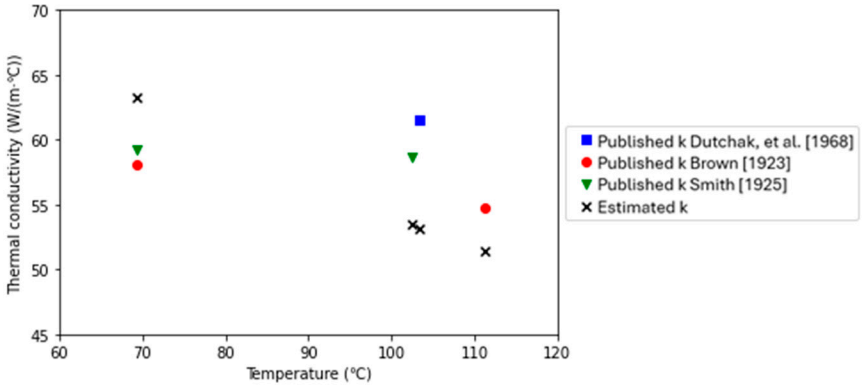


Figure 17. Comparison of the estimated solid phase thermal conductivity and the published data [31–33] for pure Tin [29].

Table 5. Comparison of estimated and published thermal conductivity data for the solid phase.

Temperature °C	Ref. Number	Av. k_Ref. W/m °C	k_Est. W/m °C	Difference %
69	[32,33]	58.64	63.22	+7.8
102	[33]	58.62	53.43	−8.9
103	[31]	61.55	53.18	−13.6
111	[32]	54.73	51.46	−5.9

The thermal diffusivity was calculated for comparison purposes using the relationship $\alpha = k/(\rho \cdot Cp)$, where the values of thermal conductivity k were obtained from [31–33], and the density ρ was obtained from [34], where it was measured using the indirect Archimedean method, with the Tin used having a purity of 99.99%. The specific heat capacity Cp was measured using adiabatic calorimetry with a relative uncertainty of 1% in estimation, with the Tin having a purity of 99.999% and published in [35]. The comparison is depicted in Figure 18 and summarized in Table 6. The maximum deviation between the estimated thermal diffusivity α and the published data falls within the range of +10.1% to −3.47%.

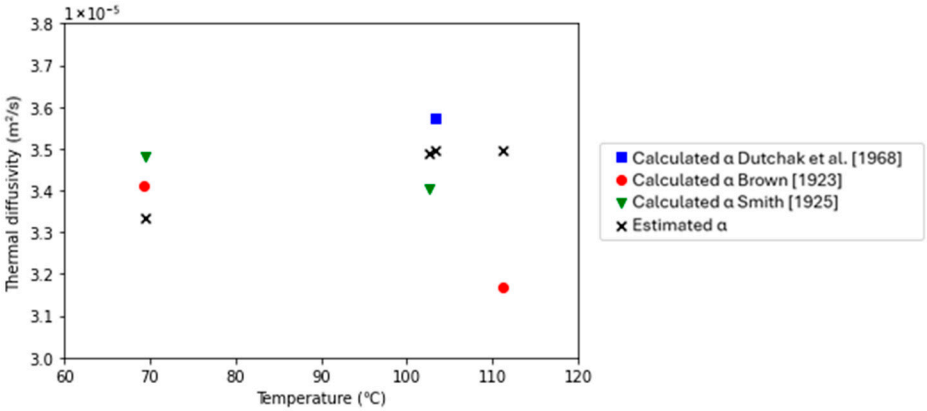


Figure 18. Comparison of the estimated solid phase thermal diffusivity and the published data [31–33] for pure Tin [29].

Table 6. Comparison of estimated and published thermal diffusivity data for the solid phase.

Temperature °C	Ref. Number	Av. α_Ref. m^2/s	α_Est. m^2/s	Difference %
69	[32,33]	3.45×10^{-5}	3.33×10^{-5}	−3.5
102	[33]	3.41×10^{-5}	3.48×10^{-5}	+2.1
103	[31]	3.58×10^{-5}	3.494×10^{-5}	−2.4
111	[32]	3.17×10^{-5}	3.49×10^{-5}	+10.1

It is worth noting that the present study involves the transient quenching of pure tin from the liquid phase, during which the latent heat released throughout solidification influences the extracted thermophysical properties. This effect is most pronounced near the solidification temperature, leading to deviations from previously reported steady-state literature data.

4.2. Estimation of Thermal Conductivity and Thermal Diffusivity for the Liquid Phase

The temperature-dependent thermal conductivity in the liquid phase was estimated and compared with data published in [31,32,36]. The thermal conductivity values in [36] were obtained via the laser flash technique with a relative uncertainty of ±(2.5–3.5) % in estimation, with the Tin having a purity of 99.998%. This comparison is depicted in Figure 19 and summarized in Table 7. The maximum deviation between the estimated thermal conductivity (k) and the published data falls within the range of +0.76% to +26.53%.

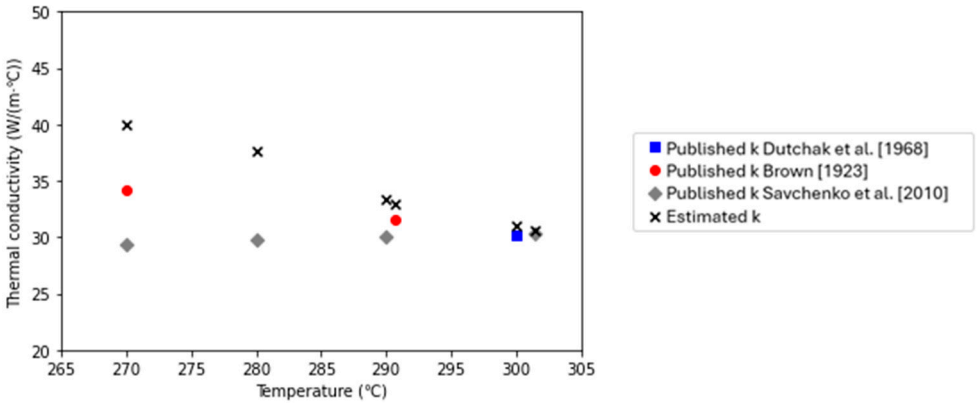


Figure 19. Comparison of the estimated liquid phase thermal conductivity and the published data [31,32,36] for pure Tin [29].

Table 7. Comparison of estimated thermal conductivity data for liquid phase pure substances with published data for pure Tin.

Temperature °C	Ref. Number	Av. k_Ref. W/m °C	k_Est. W/m °C	Difference %
270	[32,36]	31.8	40.03	+25.8
280	[36]	29.7	37.58	+26.6
290	[36]	30.1	33.33	+10.7
290.7	[32]	31.56	32.89	+7.6
300	[31]	30.16	31.06	+2.9
301.5	[36]	30.3	30.53	+0.8

The temperature-dependent thermal diffusivity in the liquid phase was estimated and compared with published data. The data was calculated using the relationship $\alpha = k/(\rho \times Cp)$, where the values of thermal conductivity (k) were obtained from [31,32], and the density (ρ) was obtained from [37] using the discharge crucible method (DC), with the tin used having a purity of 99.99%. The specific heat capacity (Cp) was measured using a differential scanning calorimeter (DSC) with a relative uncertainty of 2% in estimation, and the Tin used had a purity of 99.999%, as published in [38]. The thermal diffusivity values in [36] were obtained via the laser flash technique with a relative uncertainty of $\pm$(2.5–3.5) % in estimation, with the Tin having a purity of 99.998%. This comparison is depicted in Figure 20 and summarized in Table 8. The maximum deviation between the estimated thermal diffusivity α and the published data falls within the range of +33.71% to −4.86%.

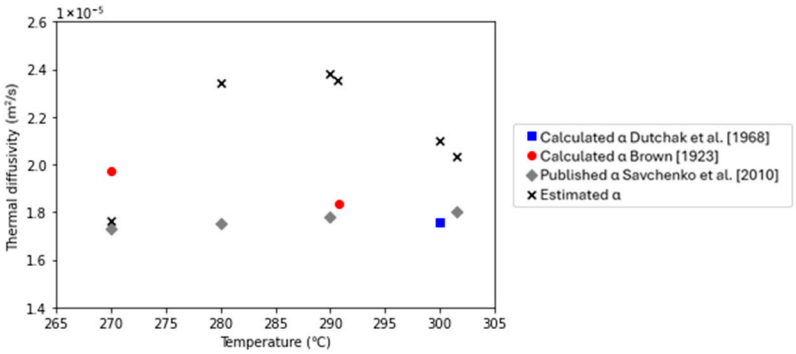


Figure 20. Comparison of the estimated liquid phase thermal diffusivity and the published data [31,32,36] for pure Tin [29].

Table 8. Comparison of estimated and published thermal diffusivity data for the liquid phase.

Temperature °C	Ref. Number	Av. α_Ref. m^2/s	α_Est. m^2/s	Difference %
270	[32,36]	1.85×10^{-5}	1.76×10^{-5}	−4.9
280	[36]	1.75×10^{-5}	2.34×10^{-5}	+33.7
290	[36]	1.78×10^{-5}	2.38×10^{-5}	+33.7
290.7	[32]	1.83×10^{-5}	2.35×10^{-5}	+28.4
300	[31]	1.76×10^{-5}	2.09×10^{-5}	+18.7
301.5	[36]	1.8×10^{-5}	2.03×10^{-5}	+12.7

4.3. Investigating the Presence of Natural Convection Within the Liquid Phase

The observed relatively large deviations in the estimated thermal diffusivity and conductivity of the liquid phase could be influenced by the development of natural convection due to the temperature gradient within the liquid sample. Natural convection, driven by temperature differences, causes fluid movement where warmer fluid rises and cooler fluid falls due to density variations. This fluid motion could disturb the temperature distribution within the liquid sample and potentially have a significant impact on the accuracy of estimated thermophysical properties for the liquid phase. To investigate the existence of natural convection in the liquid phase, a numerical simulation was conducted using ANSYS Fluent (2021R1), considering the temperature-dependent properties of pure Tin published in [39–41]. The values of pure Tin properties used in the numerical simulation are provided in Table 9.

Table 9. Values of pure Tin properties used in the numerical simulation.

Temperature °C	Thermal Conductivity W/m °C	Density kg/m^3	Specific Heat J/kg °C	Dynamic Viscosity kg/m s
249	29.60	6978	245	1.86386×10^{-3}
269	29.60	6967	244	1.78720×10^{-3}
284	29.72	6955	243	1.73793×10^{-3}
300	29.85	6943	242	1.68678×10^{-3}
319	30.34	6932	241	1.62442×10^{-3}
349	31.21	6916	239	1.53448×10^{-3}

The simulation results confirmed the presence of natural convection-induced movement within the pure Tin liquid. Figure 21 shows the velocity and temperature distributions after 1, 2, 3, and 3.5 s from the start of the cooling process, which started at 340 °C. Since the temperature measurements were taken at the center of the sample, the maximum liquid velocity at the center of the sample estimated from the numerical simulation was 0.038 m/s, which could have a significant effect on the estimated α and k of the liquid phase.

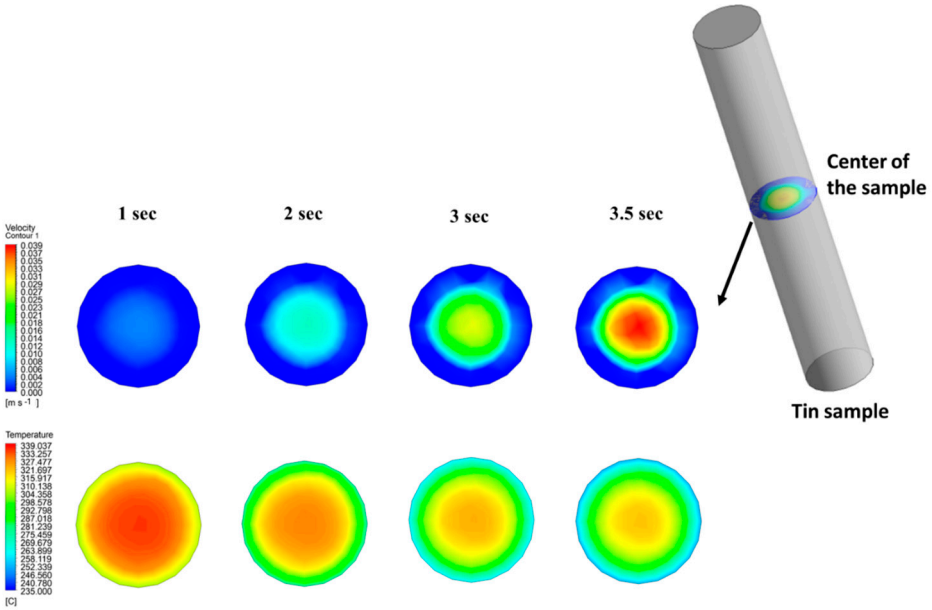


Figure 21. Natural convection in liquid tin: velocity and temperature contours [29].

A practical approach to suppress natural convection in the molten alloy is to install two perforated plates positioned above and below the thermocouple tips. These plates act as flow dampers, significantly reducing or fully eliminating buoyancy-driven fluid motion. Their design must ensure a sufficient pressure drop across the perforations; specifically, the imposed pressure drop should exceed the minimum threshold required to counteract and suppress natural convection currents within the melt.

4.4. Sensitivity Analysis

4.4.1. The Effect of the Accuracy of Thermocouple Positions on the Estimated Properties

A sensitivity analysis was carried out to quantify the effect of the accuracy of the thermocouple positions used in the inverse solver on the estimated thermal diffusivity and

conductivity. A ±1 mm uncertainty in the positions of T2 and T5 was input in the inverse solver, and the variation in the estimated values of α and k was determined.

A change of ±1 mm in the position of thermocouple T2 resulted in a ±(3.9–6.5)% deviation in the estimated solid Tin thermal diffusivity and a ±(4.3–5.9)% deviation in the estimated thermal conductivity, as shown in Figures 22 and 23.

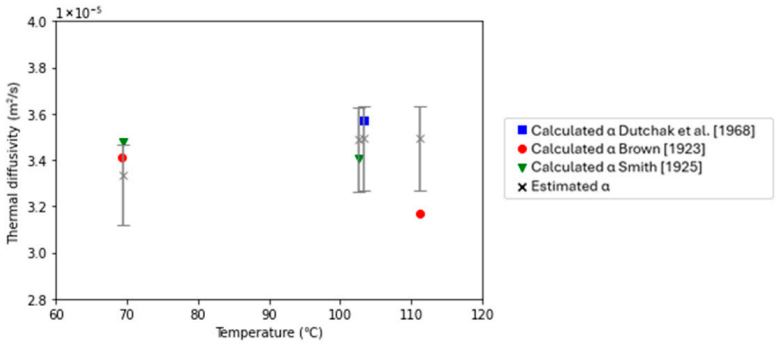


Figure 22. Effect of the uncertainty of the location of thermocouple T2 on the estimated Thermal Diffusivity [31–33] of pure Tin [29].

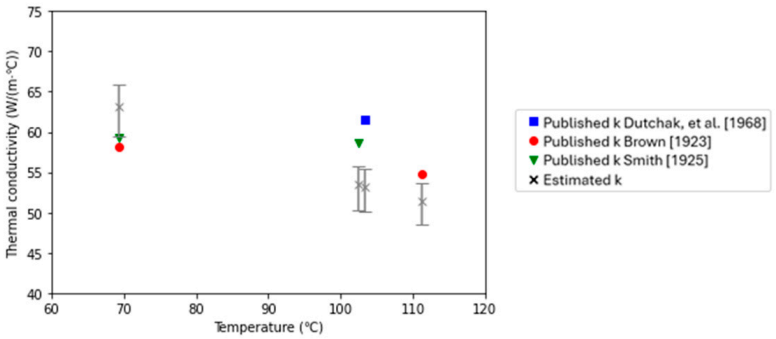


Figure 23. Effect of the uncertainty of the location of thermocouple T2 on the estimated Thermal Conductivity [31–33] of pure Tin [29].

The same change of ±1 mm in the position of thermocouple T5 resulted in a deviation of ±(10.75–11.2)% relative to the estimated α and ±(9.4–10.8)% in the estimated thermal conductivity, as shown in Figures 24 and 25.

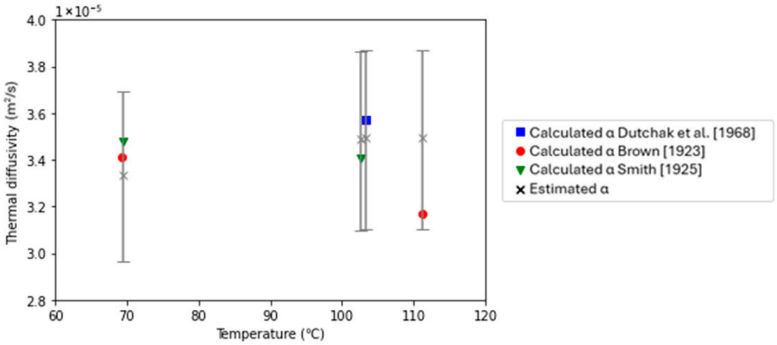


Figure 24. Effect of the uncertainty of the location of thermocouple T5 on the estimated Thermal Diffusivity [31–33] of pure Tin [29].

The results indicate that the deviation in positioning has a greater impact on the estimated thermophysical properties for T5 compared to T2, suggesting higher sensitivity near the outer surface.

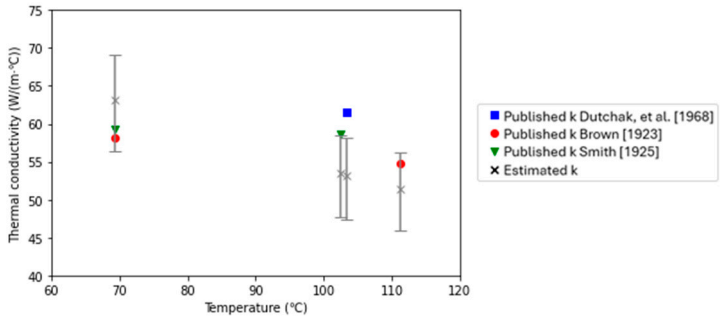


Figure 25. Effect of the uncertainty of the location of thermocouple T5 on the estimated Thermal Conductivity [31–33] of pure Tin [29].

4.4.2. Investigating Temperature Sensing System Accuracy on Thermophysical Properties Estimation

The thermocouples utilized in this study are ungrounded type K, sourced from Omega company (Norwalk, CT, USA), with a standard accuracy limit of 0.75%. The aim of this analysis was to assess the effect of the uncertainty in the temperature measurements on the estimated thermal diffusivity and conductivity. Temperature readings of thermocouples T2 and T5 were varied by introducing a ±0.75% uncertainty in the measured values. The above-noted uncertainty was introduced to the readings of T2 and T5, one at a time.

Figure 26 shows the effect of the uncertainty of ±0.75% introduced to the T2 thermocouple readings, which resulted in a relative deviation of ±(5.3–5.8)% in the estimated thermal diffusivity of the solid Tin. Similarly, Figure 27 shows a ±(4.9–5.54)% relative deviation in the estimated thermal conductivity.

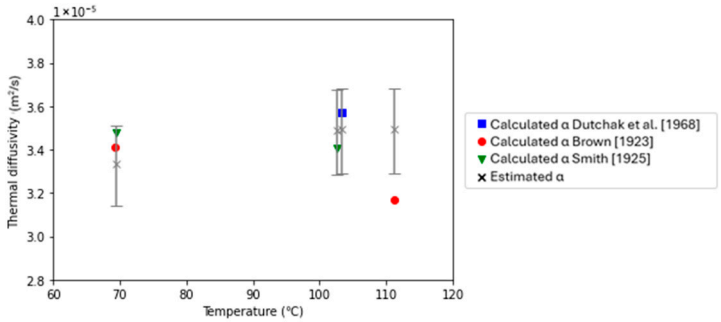


Figure 26. Effect of the uncertainty of the temperature sensing accuracy of thermocouple T2 on the estimated Thermal Diffusivity [31–33] of pure Tin [29].

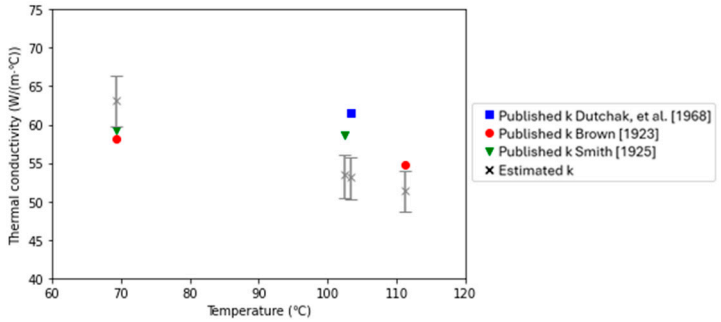


Figure 27. Effect of the uncertainty of the temperature sensing accuracy of thermocouple T2 on the estimated Thermal conductivity [31–33] of pure Tin [29].

The effect of uncertainty in the T5 thermocouple resulted in a ±(4–4.42)% relative deviation in the estimated thermal diffusivity of solid Tin and a ±(3.7–4.41)% relative deviation in the estimated thermal conductivity, as shown in Figures 28 and 29, respectively.

Overall, the results suggest that temperature-sensing accuracy has a comparable effect on the estimated thermophysical properties for both T2 and T5 thermocouples.

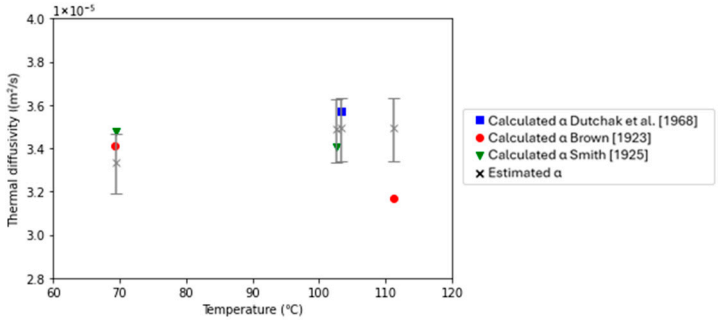


Figure 28. Effect of the uncertainty of the temperature sensing accuracy of thermocouple T5 on the estimated Thermal Diffusivity [31–33] of pure Tin [29].

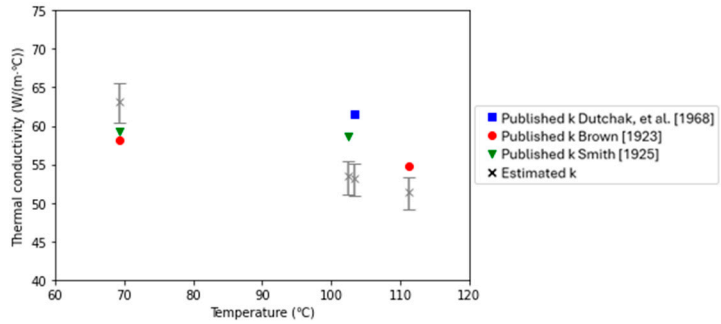


Figure 29. Effect of the uncertainty of the temperature sensing accuracy of thermocouple T5 on the estimated Thermal conductivity [31–33] of pure Tin [29].

5. Summary and Conclusions

An integrated experimental setup and inverse heat-transfer procedure were developed to quantify the thermal properties of alloy specimens subjected to rapid solidification. The accuracy of the developed experimental methodology has been examined and evaluated using pure Tin, which is considered a benchmark material, the thermophysical properties of which are readily available in the literature for both the liquid and the solid phases. The estimated solid-phase thermal diffusivity and conductivity of pure tin show reasonable agreement within the expected experimental uncertainty, with maximum deviations of +10.1% and −13.6% occurring only near the solidification interval where transient latent-heat effects influence the results. In the liquid region, the estimated thermal diffusivity and thermal conductivity showed greater discrepancies, ranging from +33.71% to −4.86% and from +0.76% to +26.53%, respectively.

The large deviations in the estimated thermal diffusivity and conductivity in the liquid phase are believed to be caused by natural convection within the liquid sample. A numerical simulation was conducted that confirmed the development of natural convection within the liquid sample. The maximum liquid velocity at the alloy sample center was estimated at about 38 mm/s.

A sensitivity study was conducted to evaluate the effects of thermocouple positioning accuracy and temperature-reading precision on the derived material properties. The uncertainty in the thermocouples' position resulted in deviations in the range of 3.9% to 11.2%, in both the estimated thermal diffusivity and thermal conductivity. The deviations due to uncertainty in the temperature readings ranged between 3.7% and 5.8% in the estimated thermal diffusivity and thermal conductivity.

Author Contributions: Conceptualization, R.B., M.S.H. and S.S.; methodology, R.B. and A.M.T.; software, R.B. and A.M.T.; validation, R.B. and A.M.T.; investigation and analysis, R.B.; resources, M.S.H. and S.S.; writing—original draft, R.B.; writing—review and editing, A.M.T., M.S.H. and S.S.; supervision, M.S.H. and S.S.; project administration, S.S. and M.S.H. All authors have read and agreed to the published version of the manuscript.

Funding: Funding for this project was provided jointly by the Ontario Centre for Innovation (OCI), OCI# 34636, McMaster University, entitled: "Characterization of an Innovative Multi-Point Fiber Optic Thermal Sensing System (FOTSS)" Program: Voucher for Innovation and Productivity (VIP) and CanmetMaterials, Natural Resources Canada (NRCan), Hamilton, ON, Canada.

Data Availability Statement: The original contributions presented in this study are included in the article. Further inquiries can be directed to the corresponding author.

Acknowledgments: We are grateful for the support and contributions from the OCI-VIP program in preparing, supporting, and funding this project. We thank Kumar Sadayappan (Research Scientist) and Gabriel Birsan (Research Engineer), both from CanmetMaterials, for their time spent with us on insightful academic discussions and contributions to the design and manufacturing of the experiment apparatus in this project.

Conflicts of Interest: The authors declare no conflicts of interest. The funders had no role in the design of the study; in the collection, analyses, or interpretation of data; in the writing of the manuscript; or in the decision to publish the results.

Abbreviations

The following abbreviations are used in this manuscript:

Nomenclature	
[a, b]	Interval range.
Cp	Specific heat, J/kg °C.
G	Sum of squares error.
H	Height, mm.
k	Thermal conductivity, W/m °C.
n	Iteration index.
N	Degree of approximate polynomial.
q_{est}	The estimated heat flux.
r	Radius, mm.
θ	General symbol refers to the value requiring estimation.
T	Temperature, °C.
Greek symbols	
α	Thermal diffusivity, m^2/s.
$[\gamma_n,\delta_n]$	Updated range in the inverse solver.
ε	Infinitesimal value (stop criteria).
m	Dynamic viscosity kg/m s.
ρ	Density, kg/m^3.
ρ cp	Volumetric heat capacity, J/m^3 °C.
ω	The golden ratio, 1.618.

References

1. King, N. Evs Forecast to Account for Two Thirds of Global Light-Vehicle Sales in 2035. Available online: https://ev-volumes.com/news/ev/evs-forecast-to-account-for-two-thirds-of-global-light-vehicle-sales-in-2035/ (accessed on 2 December 2025).
2. Razi, F.; Dincer, I. A review of the current state, challenges, opportunities and future directions for implementation of sustainable electric vehicle infrastructure in Canada. *J. Energy Storage* **2022**, *56*, 106048. [CrossRef]
3. The White House. *FACT SHEET: President Biden Announces Steps to Drive American Leadership Forward on Clean Cars and Trucks*; The White House: Washington, DC, USA, 2021.

4. Department for Transport; The Rt Hon Grant Shapps. *UK Confirms Pledge for Zero-Emission Hgvs by 2040 and Unveils New Chargepoint Design*; Department for Transport: London, UK, 2021.
5. Wazeer, A.; Das, A.; Abeykoon, C.; Sinha, A.; Karmakar, A. Composites for electric vehicles and automotive sector: A review. *Green Energy Intell. Transp.* **2023**, *2*, 100043. [CrossRef]
6. Luo, A.A.; Sachdev, A.K.; Apelian, D. Alloy development and process innovations for light metals casting. *J. Mater. Process. Tech.* **2022**, *306*, 117606. [CrossRef]
7. Lee, S.; Ham, H.J.; Kwon, S.Y.; Kim, S.W.; Suh, C.M. Thermal Conductivity of Magnesium Alloys in the Temperature Range from −125 °C to 400 °C. *Int. J. Thermophys.* **2012**, *34*, 2343–2350. [CrossRef]
8. Ozawa, T. Temperature modulated differential scanning caIorimetry-appIicabiIity and Iimitation. *Pure Appl. Chem.* **1997**, *69*, 2571–2580. [CrossRef]
9. Bazhenov, V.E.; Koltygin, A.V.; Sung, M.C.; Park, S.H.; Titov, A.Y.; Bautin, V.A.; Matveev, S.V.; Belov, M.V.; Belov, V.D.; Malyutin, K.V. Design of Mg–Zn–Si–Ca casting magnesium alloy with high thermal conductivity. *J. Magnes. Alloys* **2020**, *8*, 184–191. [CrossRef]
10. Ruoho, M.; Valset, K.; Finstad, T.; Tittonen, I. Measurement of thin film thermal conductivity using the laser flash method. *Nanotechnology* **2015**, *26*, 195706. [CrossRef]
11. Park, Y.H.; Ku, D.Y.; Ahn, M.Y.; Lee, Y.; Cho, S. Measurement of thermal conductivity of Li2TiO3 pebble bed by laser flash method. *Fusion Eng. Des.* **2019**, *146*, 950–954. [CrossRef]
12. Trofimov, A.A.; Atchley, J.; Shrestha, S.S.; Desjarlais, A.O.; Wang, H. Evaluation of measuring thermal conductivity of isotropic and anisotropic thermally insulating materials by transient plane source (Hot Disk) technique. *J. Porous Mater.* **2020**, *27*, 1791–1800. [CrossRef]
13. Rodríguez-Pérez, M.A.; Reglero, J.A.; Lehmhus, D.; Wichmann, M.; De Saja, J.A.; Fernández, A. The Transient Plane Source Technique (TPS) to Measure Thermal Conductivity and Its Potential as a Tool to Detect In-Homogeneities in Metal Foams. In Proceedings of the International Conference "ADVANCED METALLIC MATERIALS", Smolenice, Slovakia, 5–7 November 2003.
14. Zhang, Y.; Zhu, W.; Hui, F.; Lanza, M.; Borca-Tasciuc, T.; Muñoz Rojo, M. A Review on Principles and Applications of Scanning Thermal Microscopy (SThM). *Adv. Funct. Mater.* **2019**, *30*, 1900892. [CrossRef]
15. Asnin, V.M.; Pollak, F.H.; Ramer, J.; Schurman, M.; Ferguson, I. High spatial resolution thermal conductivity of lateral epitaxial overgrown GaN/sapphire (0001) using a scanning thermal microscope. *Appl. Phys. Lett.* **1999**, *75*, 1240–1242. [CrossRef]
16. Yang, I.; Kim, D. Uncertainty of thermal conductivity measurement at high temperatures using guarded hot plate apparatus. *Int. J. Heat Mass Transf.* **2022**, *198*, 123434. [CrossRef]
17. Chiba, H.; Ogushi, T.; Nakajima, H.; Torii, K.; Tomimura, T.; Ono, F. Steady state comparative-longitudinal heat flow method using specimen of different thicknesses for measuring thermal conductivity of lotus-type porous metals. *J. Appl. Phys.* **2008**, *103*, 013515. [CrossRef]
18. Monde, M.; Arima, H.; Mitsutake, Y. Analytical approach with Laplace transform to the inverse problem of one-dimensional heat conduction transfer: Application to second and third boundary conditions. *Heat Transf.-Asian Res.* **2003**, *32*, 29–41. [CrossRef]
19. Lachheb, M.; Karkri, M.; Albouchi, F.; Mzali, F.; Nasrallah, S.B. Thermophysical properties estimation of paraffin/graphite composite phase change material using an inverse method. *Energy Convers. Manag.* **2014**, *82*, 229–237. [CrossRef]
20. Trigui, A.; Karkri, M.; Pena, L.; Boudaya, C.; Candau, Y.; Bouffi, S.; Vilaseca, F. Thermal and mechanical properties of maize fibres–high density polyethylene biocomposites. *J. Compos. Mater.* **2012**, *47*, 1387–1397. [CrossRef]
21. Basily, R.; Hamed, M.; Shankar, S. On Estimating Thermophysical Properties of Liquid Metals. In Proceedings of the Fourteen International Conference on Thermal Engineering: Theory and Applications, Yalova, Turkiye, 25–27 May 2023.
22. Basily, R.; Teamah, A.M.; Hamed, M.S.; Shankar, S. Estimation of Thermo-physical Properties of Metallic Alloys. In Proceedings of the International Conference on Thermal Engineering, Tashkent, Uzbekistan, 28 May–1 June 2024.
23. Mefreh, M.; Teamah, A.M.; Shankar, S.; Hamed, M. On the Determination of Thermophysical Properties of Casting Aluminium Alloys. In Proceedings of the International Conference on Thermal Engineering, Bucharest, Romania, 18–20 June 2025.
24. Han, L.; Chen, X.; Wang, Q.; Chen, Y.; Xu, M.; Wu, L.; Chen, C.; Lu, P.; Guan, P. Neural network potential for studying the thermal conductivity of Sn. *Comput. Mater. Sci.* **2021**, *200*, 110829. [CrossRef]
25. Elsheikh, A.H.; Sharshir, S.W.; Ismail, A.S.; Sathyamurthy, R.; Abdelhamid, T.; Edreis, E.M.; Kabeel, A.E.; Haiou, Z. An artificial neural network based approach for prediction the thermal conductivity of nanofluids. *SN Appl. Sci.* **2020**, *2*, 235. [CrossRef]
26. Chauhan, R.; Sharma, S.; Pachauri, R.; Dumka, P.; Mishra, D.R. Experimental and theoretical evaluation of thermophysical properties for moist air within solar still by using different algorithms of artificial neural network. *J. Energy Storage* **2020**, *30*, 101408. [CrossRef]
27. Reoyo-Prats, R.; Grieu, S.; Faugeroux, O.; Claudet, B. A novel ANN-based method for simultaneous estimation of thermophysical properties using experimental photothermal data. *Eur. Phys. J. Appl.* **2021**, *93*, 10901. [CrossRef]
28. Trovant, M.; Argyropoulos, S. Finding Boundary Conditions: A Coupling Strategy for the Modeling of Metal Casting Processes: Part I. Experimental Study and Correlation Development. *Metall. Mater. Trans.* **2000**, *31*, 75–86. [CrossRef]

29. Basily, R. Determination of Temperature-Dependent Thermophysical Properties During Rapid Solidification of Metallic Alloys. Master's Thesis, McMaster University, Hamilton, ON, Canada, 2024.
30. Leitner, M.; Leitner, T.; Schmon, A.; Aziz, K.; Pottlacher, G. Thermophysical Properties of Liquid Aluminum. *Metall. Mater. Trans. A* **2017**, *48*, 3036–3045. [CrossRef]
31. Dutchak, Y.I.; Osipenko, V.P.; Panasyuk, P.V. Thermal Conductivity of Sn-Bi Alloys in Solid and Liquid States. *Sov. Phys. J.* **1968**, *11*, 145–147. [CrossRef]
32. Brown, W.B. Thermal Conductivities of Some Metals in the Solid and Liquid States. *Phys. Rev.* **1923**, *22*, 171–179. [CrossRef]
33. Smith, A.W. *Thermal Conductivities of Alloys*; Ohio State University Engineering Experiment Station: Columbus, OH, USA, 1925; Bulletin No. 31. Available online: https://primo.pugetsound.edu/discovery/fulldisplay?docid=alma9915074046000 1451&context=L&vid=01ALLIANCE_UPUGS:UPUGS&lang=en&search_scope=Everything&adaptor=Local%20Search%20 Engine&tab=Everything&query=title,exact,The%20Ohio%20State%20University,%20the%20Engineering%20Experiment% 20Station.%20Bulletin%20no.%2030.%20[i.e.%2031]%20October%2015,%201925.%20[Engineering%20series],AND&mode= advanced&offset=0 (accessed on 2 December 2025).
34. Wang, L.; Xian, A.-P. Density Measurement of Sn-40Pb, Sn-57Bi, and Sn-9Zn by Indirect Archimedean Method. *J. Electron. Mater.* **2005**, *34*, 1414–1419. [CrossRef]
35. Kramer, W.; Nölting, J. Anomale spezifische wärmen und fehlordnung der metalle indium. *Acta Metall.* **1972**, *20*, 1353–1359. [CrossRef]
36. Savchenko, I.; Stankus, S.; Agadjanovb, A. Measurement of Liquid Tin Heat Transfer Coefficients within the Temperature Range of 506–1170 K. *Thermophys. Prop. Mater.* **2010**, *49*, 506–511. [CrossRef]
37. Gancarz, T.; Gąsior, W.; Henein, H. Physicochemical Properties of Sb, Sn, Zn, and Sb–Sn System. *Int. J. Thermophys.* **2013**, *34*, 250–266. [CrossRef]
38. Chen, H.S.; Turnbull, D. The Specific heat of tin and gallium in their stable and undercooled pure liquid states. *Acta Met.* **1968**, *16*, 369–373. [CrossRef]
39. Chapman, T.W. The heat capacity of liquid metals. *Mater. Sci. Eng.* **1966**, *1*, 65–69. [CrossRef]
40. Rothwell, E. Copper and its Alloys in Early Times. *J. Inst. Met.* **1962**, *90*, 38–94.
41. Lucas, L. Specific Volume of Molten Metals and Alloys at Elevated Temperatures—Part 1. *Mem. Sci. Rev. Metall.* **1964**, *61*, 1–24. Available online: https://chemport-n.cas.org/chemport-n/?APP=ftslink&action=reflink&origin=npg&version=1.0&coi=1:CAS: 528:DyaF2cXktVaksbY=&md5=80a94cb2ba104c6347d3e7d4f97c76c2 (accessed on 2 December 2025).

Disclaimer/Publisher's Note: The statements, opinions and data contained in all publications are solely those of the individual author(s) and contributor(s) and not of MDPI and/or the editor(s). MDPI and/or the editor(s) disclaim responsibility for any injury to people or property resulting from any ideas, methods, instructions or products referred to in the content.